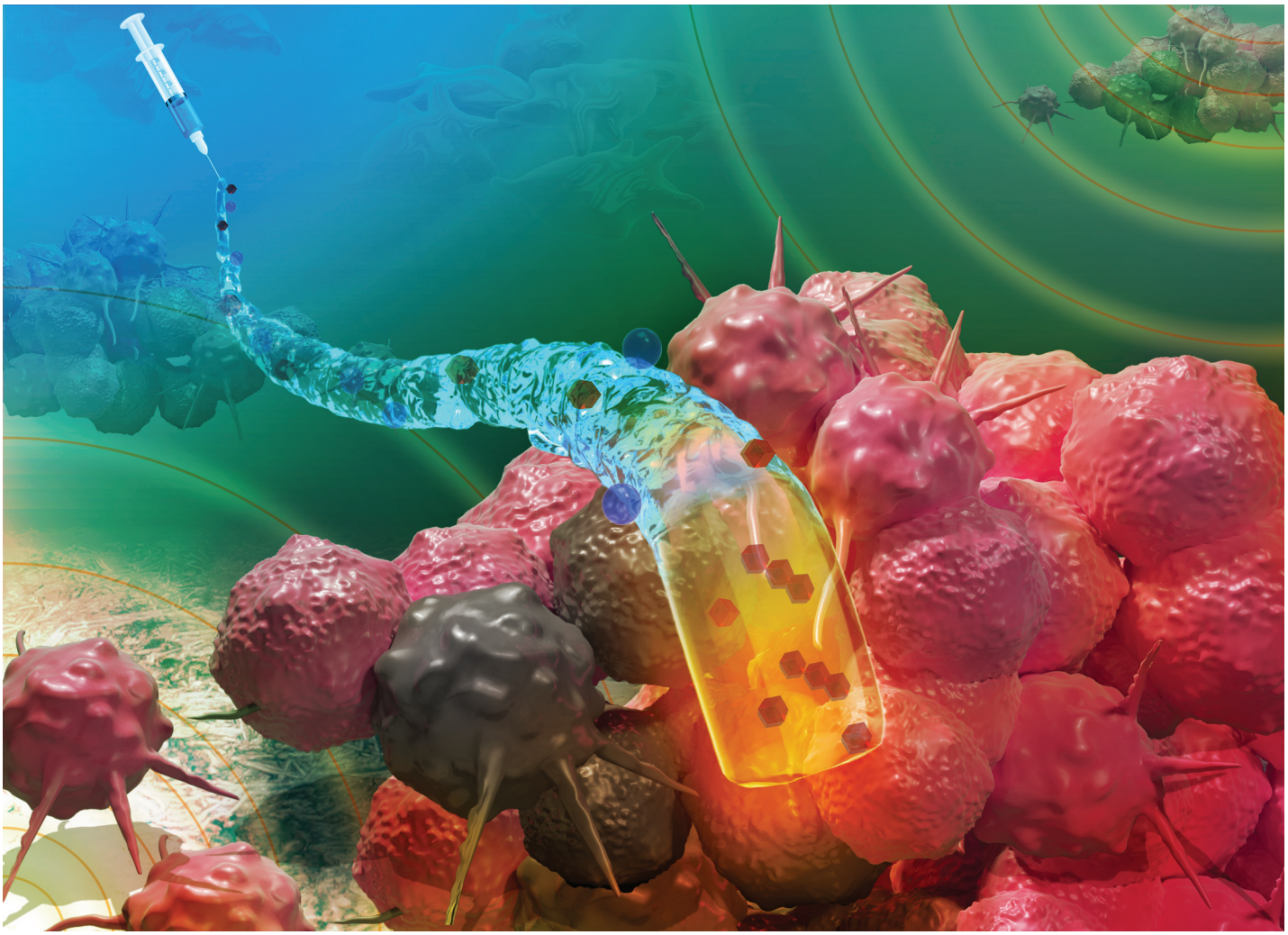

Showcasing research from the State Key Laboratory of Bioelectronics, Jiangsu Key Laboratory for Biomaterials and Devices, School of Biological Science and Medical Engineering & Collaborative Innovation Center of Suzhou Nano Science and Technology, Southeast University, Nanjing, China.

Injectable thermosensitive magnetic nanoemulsion hydrogel for multimodal-imaging-guided accurate thermoablative cancer therapy

A body temperature-induced gelation strategy is constructed for localized tumor regression based on the behaviors of magnetic nanoemulsion hydrogel (MNH) within tumors. The rapid intra-tumor gelation can restrict the MNH in tumor tissue without diffusion and leakage. The magnetic nanoparticles obtained an enhanced heat transformation effect due to linear self-assembly in the hydrogel under the ACMF. When coupled with heat accumulation *via* crosslinking among the nanoemulsion droplets, the MNH can produce large amounts of heat and raise the temperature of local tumor tissue.

As featured in:

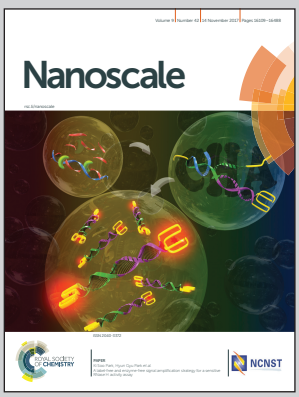

See Ning Gu, Yu Zhang *et al.*, *Nanoscale*, 2017, **9**, 16175.

ROYAL SOCIETY OF CHEMISTRY

rsc.li/nanoscale

Registered charity number: 207890

Nanoscale

PAPER

View Article Online
View Journal | View Issue

Cite this: *Nanoscale*, 2017, **9**, 16175

Injectable thermosensitive magnetic nanoemulsion hydrogel for multimodal-imaging-guided accurate thermoablative cancer therapy†

Haoan Wu,[a] Lina Song,[a] Ling Chen,[a] Yixin Huang,[b] Yang Wu,[c] Fengchao Zang,[d] Yanli An,[d] Hanbai Lyu,[a] Ming Ma,[a] Jun Chen,[c] Ning Gu *[a] and Yu Zhang *[a]

Received 22nd April 2017,
Accepted 22nd July 2017

DOI: 10.1039/c7nr02858j

rsc.li/nanoscale

Ferrofluid-based magnetic hyperthermia of cancers has gained significant attention in recent years due to its excellent efficacy, few deleterious side effects and unlimited tissue penetration capacity. However, the high tumor osmotic pressure causes injection leakage and thus position imprecision because of the fluidity of the ferrofluid and the absence of multimodal imaging guidance, which create tremendous challenges for clinical application. Here, a body temperature-induced gelation strategy is constructed for accurate localized magnetic tumor regression based on the unique behaviors of a magnetic nanoemulsion hydrogel (MNH) within tumors. The rapid intra-tumor gelation can securely restrict the MNH in tumor tissue without diffusion and leakage. The magnetically induced nanoparticle assembly-enhanced heating in the hydrogel and the heat accumulation caused by crosslinking among the nanoemulsion droplets further increased the heating efficiency. Meanwhile, US/MR/NIR multimodal imaging can guide the whole therapeutic process, achieving excellent magnetic hyperthermia therapeutic efficiency. This work highlights the great promise for improving the magnetic hyperthermia efficiency and the precision of the injection site for localized tumor therapy.

Introduction

Hyperthermia has become a new therapeutic procedure after surgical therapy, chemotherapy and radiotherapy in current cancer treatment.[1] Magnetic nanoparticle-mediated hyperthermia is to apply an alternating magnetic field of sufficient strength and frequency to cause the particles to heat by the combined effects of the rotational external (Brownian) and internal (Néel) diffusion of the particle magnetic moment.[2,3] The limitations of penetration depth into body tissues by microwave, laser and ultrasound energy severely restrict their further *in vivo* application and fast clinical translation.[4] Magnetic hyperthermia based on the specific physical feature of magnetic nanoparticles under the adopted radiofrequency electromagnetic field is one of the ideal platforms for on-demand treatment of biological objects.[5–7] Moreover, alternating current magnetic field (ACMF) can exert rare side effects on the body, providing the potential to target tumors in various organs.[8,9]

Nevertheless, in the case of magnetic hyperthermia applications, intravenously injected magnetic nanoparticles tend to have high accumulation in the liver and spleen, resulting in inadequate tumor accumulation for a sufficient temperature increase.[3,10] Repetition of thermal treatments with a high concentration of magnetic nanoparticles or using high magnetic field amplitude (H) and frequency (f) may cause a concomitant potential side-effect.[11–13] For *in situ* localized tumor treatment, intra-tumor injection of ferrofluid may be technically feasible.[14,15] However, when magnetic nanoparticles are administered directly into the tumor, the small particulate size and the high tumor osmotic pressure make them easily leak out along the route of the syringe needle and escape from the tumor tissues during the long-term therapeutic process (Fig. S1†).[16,17] Therefore, tumor tissue cannot receive effective therapy while tissues around the tumor are heated. Furthermore, the relatively low SAR values of Fe_3O_4 nanoparticles restrict their potential application in cancer hyperthermia *in vivo*. At the same time, the lack of multimodal

[a]*State Key Laboratory of Bioelectronics, Jiangsu Key Laboratory for Biomaterials and Devices, School of Biological Science and Medical Engineering & Collaborative Innovation Center of Suzhou Nano Science and Technology, Southeast University, Nanjing 210096, P. R. China. E-mail: zhangyu@seu.edu.cn*
[b]*CAS Key Laboratory for Biological Effects of Nanomaterials & Nanosafety, National Center for Nanoscience and Technology, Beijing 100190, P. R. China*
[c]*Jiangsu Province Tumor Hospital, Nanjing 210009, P. R. China*
[d]*Jiangsu Key Laboratory of Molecular and Functional Imaging, Medical School, Southeast University, Nanjing 210009, P. R. China*

†Electronic supplementary information (ESI) available: Details of materials used, characterization, thermal response gelation performance *in vitro*, animal protocol, *in vivo* ultrasound imaging, *in vivo* MR and NIRF imaging, *ex vivo* histological staining. See DOI: 10.1039/c7nr02858j

imaging guidance makes it hard to realize real-time visualization of the location and distribution of the nanoparticles in the tumor, and to monitor the treatment efficacy.[18–21]

Poly(ethylene glycol) diacrylate (PEG-DA), as one of the well-known synthetic polymers, has been extensively used in biomedical applications.[22] The end groups of PEG-DA, acrylates, can act as bridging agents and insert into the oil/water droplet interface with increasing temperature, causing powerful inter-droplet attractions to induce gelation of the nanoemulsion.[23] It was found that Zn ferrite magnetic nanoparticles (MNPs) and indocyanine green (ICG) can be uniformly dispersed or dissolved into o/w nanoemulsions. On this ground, we herein present a smart injectable and thermosensitive magnetic nanoemulsion hydrogel (MNH) containing Zn ferrite MNPs, PEG-DA, ICG and silicone oil droplets dispersed in an aqueous continuous phase for localized magnetic thermal ablation of tumors under multimodal imaging guidance. MNH injected into the tumor tissues is transformed into a solid-like magnetic hydrogel without leakage in response to body temperature (37 °C). By applying the ACMF, the tumors are expected to achieve coagulative necrosis by magnetic nanoparticle-induced thermal ablation. The procedure of *in situ* injection could be real-time and dynamically monitored by ultrasound (US) imaging, while the therapeutic process was guided and evaluated by the enhanced magnetic resonance (MR) imaging and near-infrared fluorescence (NIRF) imaging (Scheme 1).

To the best of our knowledge, this is the first report on the thermosensitive transition from a low-viscosity liquid to a solid-like colloidal gel for localized tumor thermal therapy by the combination of magnetic nanoparticles and an oil-in-water nanoemulsion. Differing from the traditional ferrofluid pattern, such a special localized therapeutic hydrogel features the following advantages: first, the body temperature responsive MNH enables *in vivo* tumor thermal ablation without spillage along the route of the syringe needle during the injection process. Furthermore, within the MNH, Zn ferrite MNPs as used enhanced the heat transformation effect at a very low magnetic nanoparticle dosage (Fe: 90 μg), which is attributed to its high SAR values and the local orientation in the hydrogel materials under the ACMF. The crosslinking among the nanoemulsion droplets further increased the heat accumulation. In addition, Zn ferrite MNPs, ICG and the nanoemulsion act as high-performance contrast agents for MR imaging, NIRF imaging and US imaging, respectively; therefore the accurate location of the solid-like MNH can be monitored. Last but not least, compared with intravenous or percutaneous injection of ferrofluids, the topical administration of Zn ferrite MNPs packaged within the nanoemulsion crosslinked network guaranteed better *in vivo* biosafety. All these benefits cause the efficient tumor hyperthermia therapeutic outcome. Nanoemulsions can also provide efficient encapsulation and delivery of hydrophobic anticancer drugs, if necessary. This technique works for the treatment of small, unrespectable tumors or for patients who are poor surgical candidates. For example, gliomas are a suitable choice because surgical resection of gliomas is difficult to do and the residual tumors tend to relapse.

Results and discussion

Synthesis and characterization of magnetic nanoemulsion hydrogel (MNH)

Zn ferrite MNPs with an average diameter of 15 nm [transmission electron microscopy (TEM) image, Fig. 1(a)] were prepared *via* a thermal decomposition approach in the organic phase. High-resolution transmission electron

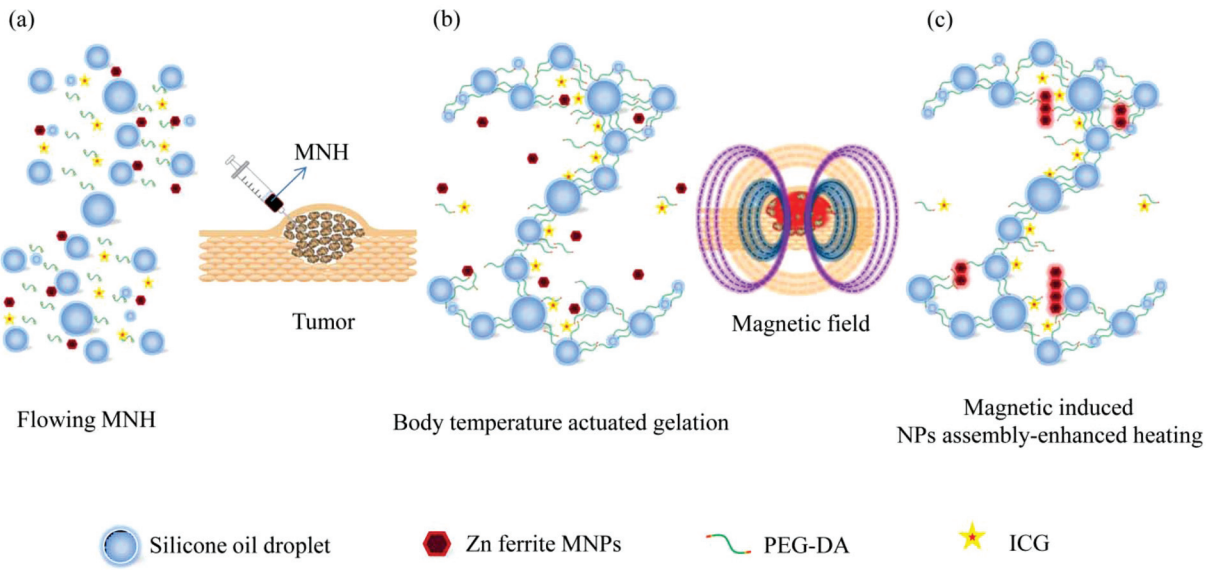

Scheme 1 Schematic illustration of the microstructure and application of the MNH. (a) Flowing low-viscosity liquid MNH *in vitro* (<25 °C). (b) Temperature increase-actuated colloidal gelation of the nanoemulsion droplet through PEG-DA bridging attraction. (c) Magnetic-induced NP assembly-enhanced heating for tumor thermal ablation.

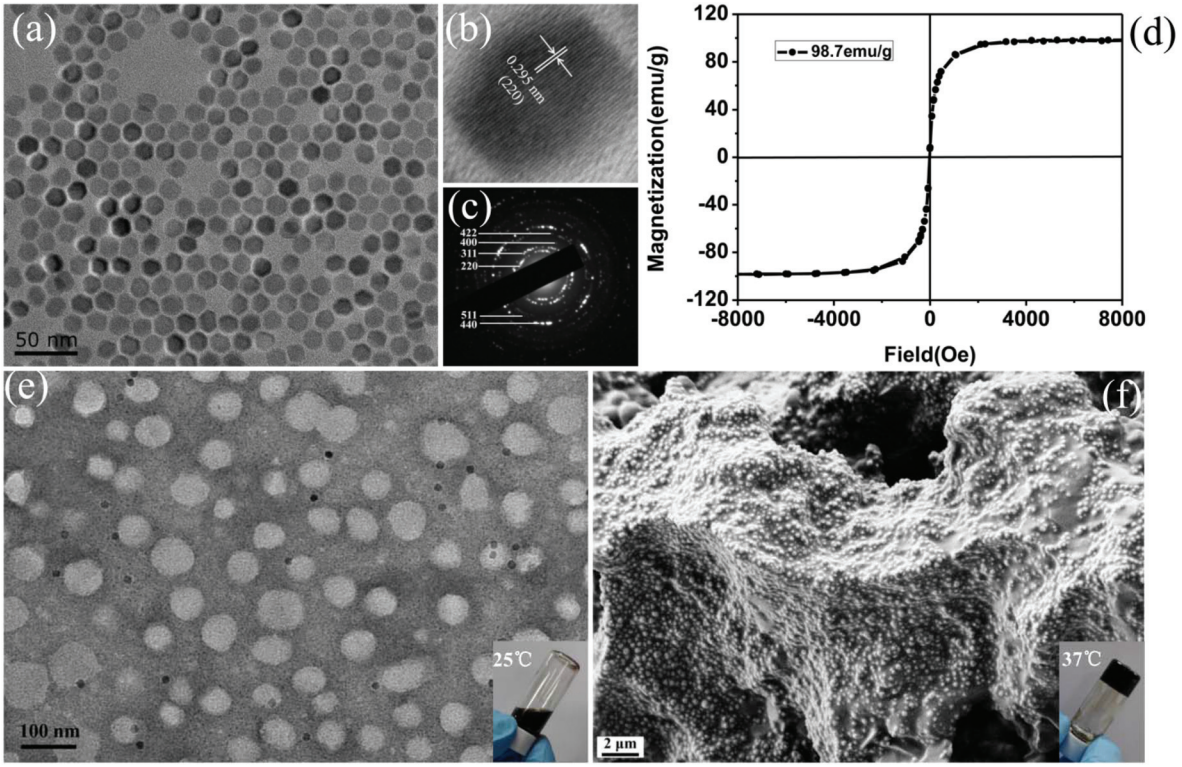

Fig. 1 (a) TEM image, (b) HRTEM image and (c) corresponding SAED pattern of Zn ferrite nanoparticles. (d) Hysteresis loops of Zn ferrite nanoparticles measured at 300 K. (e) Negatively stained TEM image of the MNH taken at 25 °C. (f) SEM image of MNH taken at 37 °C. Inset: Photographs of the sample taken 5 min after equilibration at the corresponding temperatures indicated.

microscopy [HRTEM, Fig. 1(b)] analysis and the selective area electron diffraction [SAED, Fig. 1(c)] patterns indicate that the nanoparticles have high-quality crystallinity. Fig. S2† shows the scanning electron microscopy (SEM) image of Zn ferrite nanoparticles with uniform size and regular arrangement. The Zn^{2+} dopant substitution strategy for metal ferrite nanoparticles has been pursued to achieve high and tunable nanomagnetism.[24] To identify the Zn element, the corresponding element mapping and composition measured by energy dispersive spectrometer (EDS) are shown in Fig. S3.† Magnetic measurements using a vibrating sample magnetometer (VSM) at room temperature (300 K) showed that the obtained nanoparticles exhibit a higher magnetization value [98.7 emu g^{-1} Fe, Fig. 1(d)] in comparison with that of conventional Fe_3O_4 nanoparticles (56 emu g^{-1} Fe, a commercial product of Ferumoxytol). The microstructure and composition of MNH before and after gelation were visualized by electron microscopic observation. Negative-stained TEM was performed to observe the morphology and distribution of nanoemulsion droplets and Zn ferrite MNPs taken from the liquid sample. Fig. 1(e) shows that Zn ferrite MNPs are evenly dispersed in the nanoemulsion and tend to distribute around the nanoemulsion droplets due to their high surface energy (Fig. S4†). Under the induction of heat, effective interdroplet attractions were generated among adjacent nanoemulsion droplets through PEG-DA bridging (Fig. S5†) and the nanoemulsion droplets merged to become larger size droplets [Fig. 1(f)]. The corresponding element mapping and composition measured by EDS (Fig. S6†) exhibit the uniform distribution of Fe element within the nanoemulsion gel frameworks, indicating the good dispersibility of Zn ferrite MNPs within the MNH after the gelation process.

To further probe the gelation process, rheological experiments including dynamic temperature sweeps were conducted to explore the viscoelasticity of the nanoemulsion hydrogel under small amplitude oscillatory shear. Fig. 2(a) shows the elastic and loss moduli G' and G'', respectively, of a relative canonical gelling nanoemulsion during a temperature ramp from 20 °C to 50 °C. At a body temperature of 37 °C, $G' \approx G''$, indicating the gel temperature, T_{gel}. Fig. 2(b) shows corresponding viscosities obtained at specific temperatures. MNH with low viscosity below the gel temperature allowed for convenient injection through syringes. After the gelling occurs, MNH can form an *in situ* implant in tumor tissue due to its high viscosity and MNH will tightly adhere to the tumor tissue when the temperature reaches 60–65 °C (Fig. S7†). As the temperature rises further, the strength of the MNH also increases (Fig. S8†). Dynamic light scattering (DLS) data show that nanoemulsion droplets have an average hydrodynamic size of 55 nm [Fig. 2(c)] with a narrow size distribution, and no obvious size change occurred over a period of several weeks owing to suppressed coalescence at small droplet diameters.[25]

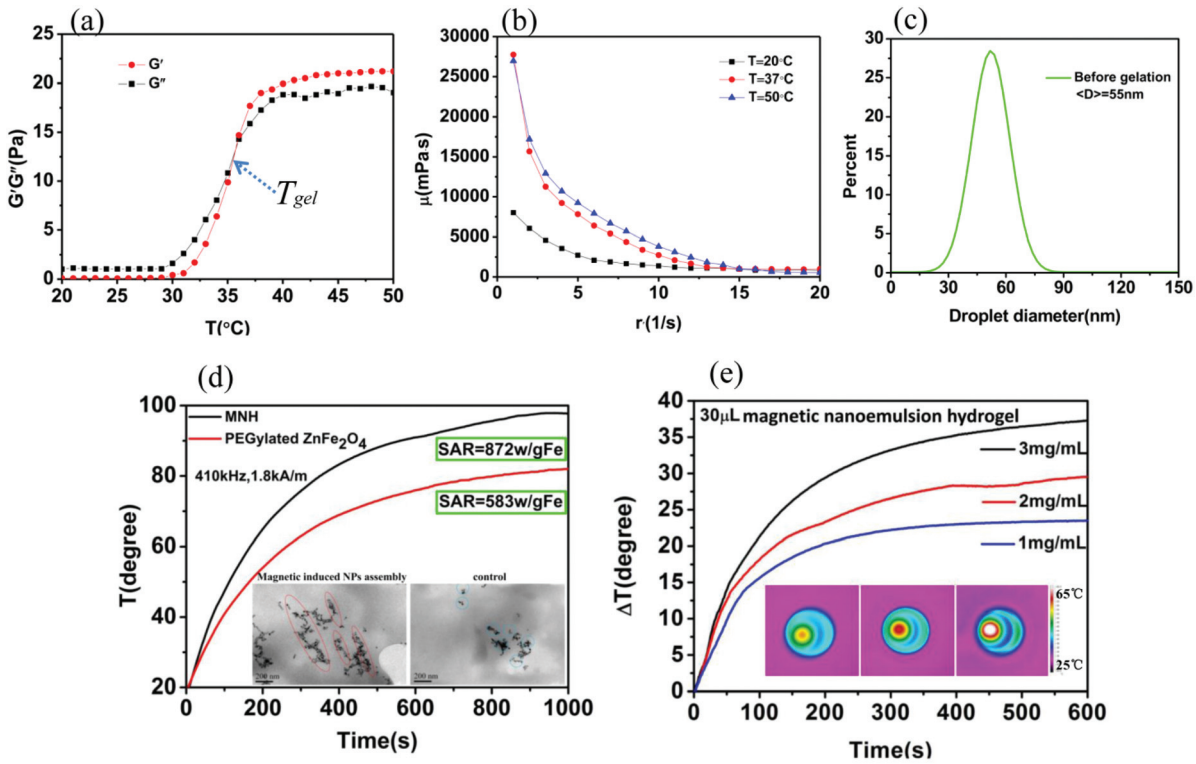

Fig. 2 (a) Thermal rheology of the sample from 20 °C to 50 °C, indicating the gel temperature, T_{gel}. (b) Viscosity change of the MNH at specific temperatures; *r* represents the rotor speed. (c) DLS sizes measurement of MNH before gelation. (d) Time-temperature curves of MNH and PEGylated Zn ferrite nanoparticles in aqueous phase with the same 1.7 mg Fe mL^{-1} under ACMF (410 kHz, 1.8 kA m^{-1}). (e) Fe concentration-dependent temperature elevations of 30 μL MNH under ACMF (410 kHz, 1.8 kA m^{-1}). Inset: The corresponding thermal images at 300 s measured inside the coil.

In vitro magnetic heating performance

The excellent magnetic induction heat of MNPs in an ACMF could be evaluated by the SAR value, which was highly dependent on magnetic relaxation and was proportional to the M_s value.[26] The MNH and PEGylated[27] Zn ferrite MNPs in aqueous solution with the same Fe concentration of 1.7 mg mL^{-1} (1 mL) induced temperature elevation by ≈80 and 61 °C by applying an ACMF (410 kHz, 1.8 kA m^{-1}) for 15 min and possessed SAR values of 872 and 583 W g^{-1} Fe, respectively [Fig. 2(d)]. Compared to the PEGylated Zn ferrite MNPs, MNH has better heating performance, which may be attributed to the local orientation of MNPs under the ACMF and the accumulation of heat in the nanoemulsion gel network (Fig. S9†). For the local orientation of Zn ferrite MNPs in hydrogel under the ACMF, Bio-TEM and frozen sections were taken to observe the microscopic structure of the MNH, where gelation occurred in a water bath as a control. As shown in the inset of Fig. 2(d), the Bio-TEM image shows orientated nanoparticle assemblies in the gel along the magnetic field direction, which were not present in the gel formed by water bath. Prussian blue staining images of a frozen section from the MNH in which gelation occurred upon exposure to ACMF revealed that the assemblies were composed of orientated particle aggregates, while the gelation that occurred in the water bath resulted in a chaotic state of particle aggregates (Fig. S10†). The orientated assemblies of Zn ferrite MNPs induced under the magnetic field enhance the magnetic interaction between the nanoparticles and increase the thermogenesis of MNH more than that of the PEGylated Zn ferrite MNPs in aqueous solution, as demonstrated in our previous work.[28]

The magnetic thermal performance of MNH was further evaluated *via* dosage simulation, where 30 μL of MNH was used with three different concentrations of Fe. As shown in Fig. 2(e), temperature increases of 32.5, 26.5, and 22 °C could be realized after 5 min application of an ACMF (410 kHz, 1.8 kA m^{-1}) at Fe concentrations of 3.0, 2.0, and 1.0 mg mL^{-1}, respectively. Such an excellent *in vitro* heating effect of MNH is expected to highly favor the further *in vivo* magnetic thermal ablation of tumors. In addition, our designed mid-frequency ACMF of 1.8 kA m^{-1} at 410 kHz has been demonstrated to be safe and beneficial for potential application.[29–31]

In vivo multimodal-imaging-guided efficient magnetic hyperthermia

Encouraged by the *in vitro* thermal effect of MNH, we then investigated the feasibility of using MNH for *in vivo* magnetic hyperthermia and US/MR/NIRF imaging in the 4T1 tumor-xenograft model. When the tumor in mice reached a size of about 60 mm^3, the mice were treated by intratumoral injection with MNH (3 mg mL^{-1}, 30 μL) due to its high fluidity. In

response to the body temperature, the liquid MNH quickly changed into its solid-like state without leakage [Fig. 3(b)]. MNH could be directly injected into the core position of the tumor in a minimally invasive manner under the guidance of *in situ* US imaging. As shown in Fig. 3(a), the *in vivo* US signals give a significant increase in intensity during the injection process of MNH into the tumor centers, indicating that the injection site could be precisely positioned *via* US imaging. Then, the tumor region of mice is placed into the center of a water-cooled magnetic induction copper coil with appropriate size (3 cm in diameter and 1.5 cm in length, Fig. S11†) and the hyperthermia process was monitored *in situ via* taking thermal images with an infrared camera [Fig. 3(c)]. As shown, the local tumor temperature rapidly reached more than 60 °C after 120 s application. Amazingly, the high temperature area spread quickly and covered almost the whole tumor site within 300 s, while only a few degrees increase was observed in the normal tissue around the tumor due to its rapid heat dissipation compared to that of tumor tissue during the short treatment time of 5 minutes. The resulting temperature (above 60 °C) was previously shown to be high enough to cause irreversible tumor tissue damage and coagulative necrosis,[32] while less thermal damage occurred for the surrounding normal tissue.

MR imaging allowed visualization of the localization of MNH in the tumor. As shown in MR images [Fig. 3(d)], the *T*2-weighted MR signal intensity of the tumor was locally decreased significantly 2 min after injection of the MNH and maintained such a low signal intensity for a long time. To confirm the location of the MNH within the tumor, *T*2*-weighted MR images before and after magnetic thermal therapy were obtained. We can see that MNH was a black spot in the tumor tissue, which remained fixed in position within 10 minutes. After 2 hours of hyperthermia, there was no obvious spread of the black spot. The results demonstrated that the MNH stayed in the tumor center after being injected into the tumor tissue and that the MNH remained in the

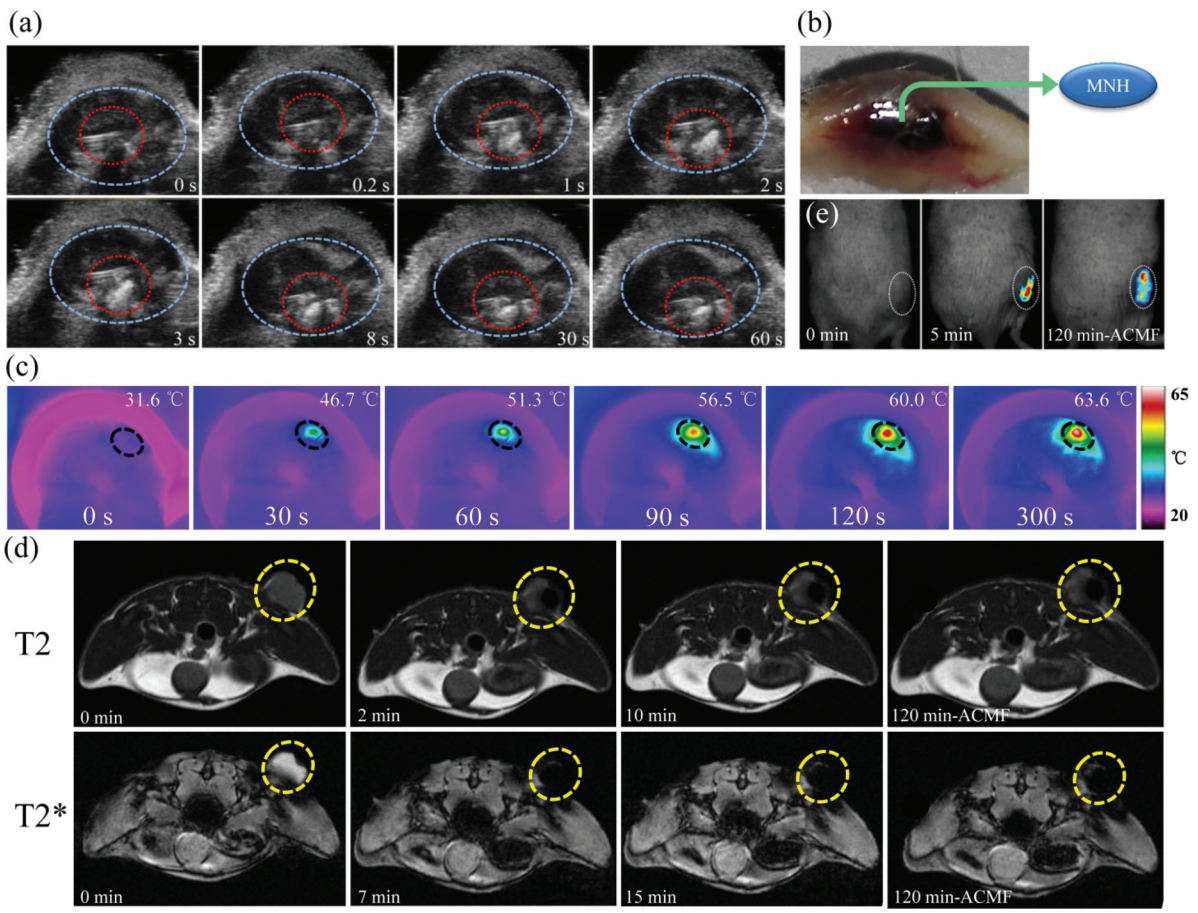

Fig. 3 (a) *In vivo* ultrasound imaging before (0 s) and after (0.2 s, 1 s, 2 s, 3 s, 8 s, 30 s and 60 s) the *in situ* administration of MNH; blue and red dashed circles indicate tumor and MNH, respectively. (b) Digital photos of tumor section after injection of MNH without ACMF. (c) *In vivo* thermal images of mice inside the copper coil under ACMF (410 kHz, 1.8 kA m^{-1}) after *in situ* implanting MNH for varied durations. The black dashed circles indicate the tumor. (d) *T*2 and *T*2*-weighted MR images of tumor-bearing mice acquired before and at different time points after injection of MNH and 2 h after exposure to ACMF. Yellow circles indicate tumor sites. (e) *In vivo* NIRF imaging of 4T1 tumor mice injected with MNH in 0 min, 5 min (without ACMF) and 120 min (after exposure to ACMF). The white dashed circles indicate the tumor.

initial position of the tumor without diffusion and penetration after the application of ACMF. The PEGylated Fe_3O_4 solution tended to spread to the surrounding normal tissue (Fig. S12†).

NIRF imaging was employed to guide the intratumoral injection and evaluate the fluorescence properties of the MNH before and after magnetic thermal therapy [Fig. 3(e)]. Five minutes after injection, the fluorescence imaging shows that MNH accumulated in the tumor area through the thermosensitive *in situ* gelation effect [Fig. 3(e), middle]. An expanded NIRF signal was observed in the tumor area at 2 h post application of an ACMF, indicating the relatively stable gelation of MNH in tumor tissue and partial diffusion of small-molecule ICG under the induction of heat [Fig. 3(e), right], which implied the potential for promoting diffusion of loaded anticancer drug within tumor tissue by ACMF.

In vivo antitumor efficacy

Finally, the *in vivo* anticancer efficiency of MNH after a single magnetic ablation was evaluated by recording the tumor volume and survival rate within the treatment duration [Fig. 4(a) and (b)]. Compared to the sharply increased tumor volume of the untreated, normal saline (NS) and MNH without magnetic field groups, the MNH implanted tumor treated with magnetic field shrank significantly and then the tumor almost disappeared after 3 d feeding. The left black scars at the original tumor sites were completely healed after one month feeding (Fig. $4w_4$) and not a single death nor tumor reoccurrence was observed in the following 3 months (Fig. S13†), whereas most of the mice in the control groups showed average life spans of 12–40 days from the beginning of treatment. Prussian blue/nuclear fast red (PB&NFR) double staining and hematoxylin & eosin (H&E) double staining of tumor regions were also carried out to further evaluate *in vivo* microscopic therapeutic outcomes [Fig. 4(c)]. From the PB&NFR double staining results, we found the blue spots representing the Zn ferrite MNPs dispersed in tumor tissue. Compared to the cancer cell damage with nuclear membrane fragmentation by the application of ACMF, no significant damage was found in the control groups. H&E staining indicates that the cell nucleus has been destroyed in the hyperthermia group, while the cell nucleus in the control group was clear and complete. The pathological analysis strongly demonstrated the good therapeutic efficiency of MNH by the application of ACMF. The PB&NFR staining image of border parts between tumor tissue and normal tissue shows no obvious damage to the surrounding tissue (Fig. S14†). The longer term *in vivo* safety analysis from H&E staining of the major organs on day 28 (Fig. S15†) shows no obvious pathological tissue damage or abnormality

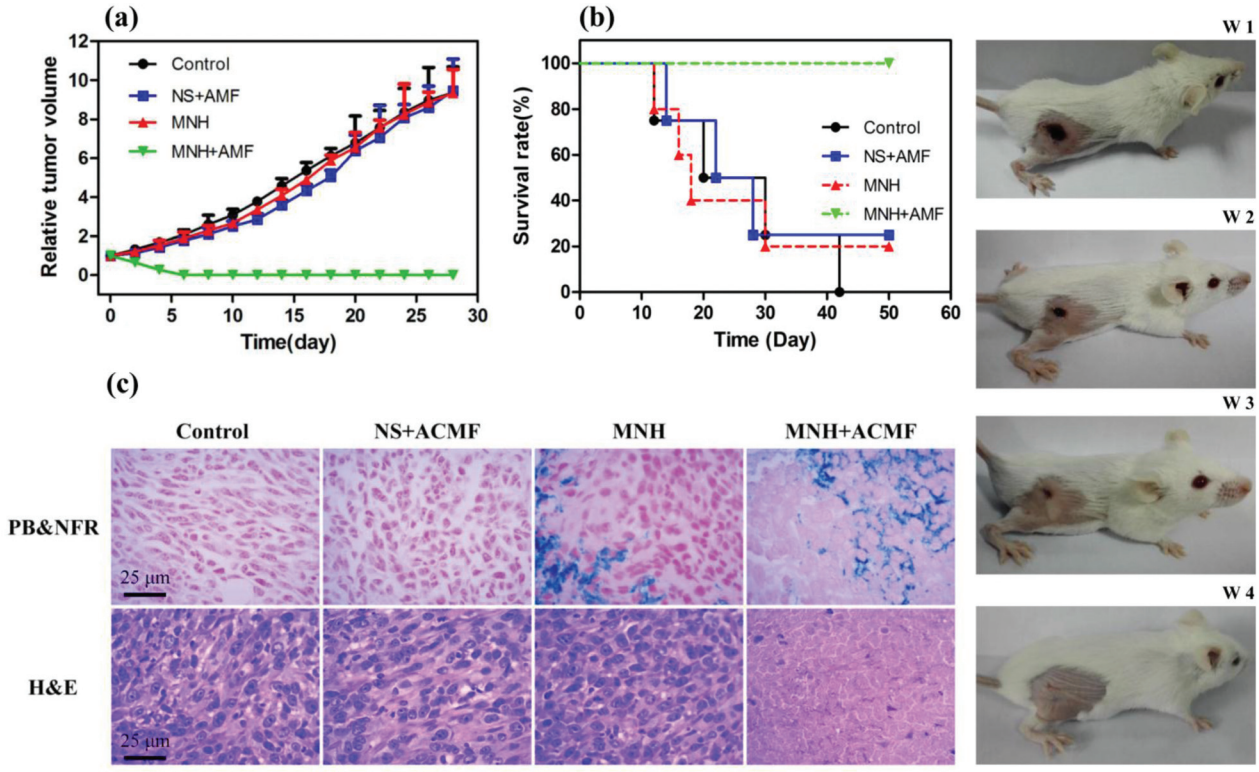

Fig. 4 (a) Tumor growth profiles of 4T1 tumors after several treatment processes as indicated. Tumor volumes were normalized to their initial sizes. Error bars represent the standard deviation of 6–8 mice per group. (b) The long-term survival rate of mice bearing 4T1 tumor after different treatments. (c) PB&NFR double staining and H&E staining images of tumor sections harvested from various groups of 4T1 tumor-bearing mice at 5 h after application of ACMF. Image c is ×400 magnification. Panels (w_1–w_4) show the digital photos of MNH-implanted 4T1 tumor-bearing mice after single exposure to ACMF for extended days.

within major organs of mice, further indicating that the administrated MNH dosage will not cause serious side effects to normal tissues.

Experimental

Oleic acid (OA)-coated Zn ferrite MNPs synthesis

The OA-coated Zn ferrite MNPs were synthesized *via* a thermal decomposition method. In a typical experiment, $Fe(acac)_3$ (2 mmol) and $Zn(acac)_2{\cdot}H_2O$ (1 mmol) were dissolved in 20 mL of benzyl ether containing 10.5 mmol OA and 1.5 mmol OAm. They were mixed and stirred under a flow of N_2. The mixture was heated up from room temperature to 220 °C at a heating rate of 3.3 °C min^{-1} and maintained at this temperature for 1 h. Then, the mixture was heated to 290 °C with a uniform heating rate and refluxed for 30 min. At last, the black-brown solution was precipitated through magnetic separation, washed with ethanol three times, and then dispersed in chloroform.

Preparation of oil-in-water magnetic nanoemulsion hydrogel (MNH)

MNH was prepared by the following two steps. In step one, 345.6 mg of SDS was dissolved in 20 mL of distilled water, which served as the water phase. The oil phase was mixed to yield chloroform solutions that contained 2 mL of silicone oil, and 18 mg of OA-coated Zn ferrite MNPs. Subsequently, the oil phase was added into the boiling water dropwise under continuous stirring. The preparation was concentrated to 4 mL, which gave the crude emulsion. Finally, the crude emulsion was homogenized by sonication for 30 min (Ultrasonic Homogenizer JY92-IIN, 20–25 kHz, 650 W, Ningbo Scientz Biotechnology Co. Ltd). In step two, 2 mL of PEG-DA was added into the above-mentioned nanoemulsion dropwise under continuous vortexing, and ultrasound was used to make it sufficiently dispersed in the magnetic nanoemulsion. Then, we obtained the final product MNH, which was then stored at 4 °C for further experiments.

In vitro heat induction measurements

Measurement of heat generation of MNH *in vitro* was carried out using a moderate radio frequency heating machine (Shuangping SPG-06-II, China). The samples at uniform concentration were placed inside a copper coil under an alternating current magnetic field (ACMF). The specific absorption rate (SAR) is defined as the amount of heat generated per unit gram of magnetic material per unit time, and highly determines the heating ability of MNH when an ACMF is applied (410 kHz, 1.8 kA m^{-1}). The SAR value of MNH is calculated with the following formula: $SAR = C_w(dT/dt)\ (m_s/m_{Fe})$, where C_w is the specific heat capacity of the suspension (specific heat capacity of water is 4.18 kJ kg^{-1} K^{-1}); dT/dt is the initial slope of temperature *versus* time curves; m_s is the mass of the suspension; and m_{Fe} is the mass of the magnetic material in the suspension.

In vivo magnetic ablation of tumors

4T1 xenografted tumor mice were randomly divided into 4 groups when the tumor diameter reached ~0.5 cm (n = 8 per group). Then, mice were *in situ* administrated with 30 μ of MNH after being immobilized on the plate. All *in vivo* magnetic-induced hyperthermia experiments were carried out safely using a moderate radio frequency heating machine (Shuangping SPG-06-II, 410 kHz, 1.8 kA m^{-1}, China). The mice were placed into the induction coil using a specially designed Teflon supporter so that tumors were located exactly in the region of the ACMF possessing the highest field density. Thermal images of mice were taken using an infrared-thermograph (Fulke, Ti32, USA) for temperature measurements. Meanwhile, mice *in situ* administrated with 30 μL of MNH without ACMF or 30 μL of saline were used as controls. The tumor volumes were calculated from the formula: $V = AB^2\pi/6$, where A is the longer and B is the shorter lateral diameter of the tumor. Relative tumor volumes (ΔV) were calculated as $V - V_0$ (V_0 represents the tumor volume when the treatment was initiated); body weight, tumor appearance, and survival rate (by dividing the number of surviving mice by the number of total mice at the initial of treatment, *i.e.*, 8) of each mouse in different groups were also evaluated.

Conclusions

In summary, we have successfully developed a novel approach for localized cancer regression by accurate magnetic thermal ablation under the guidance of multi-modality imaging. The body temperature-responsive phase-transformation strategy was introduced to solve the typical difficulties of low therapeutic and imaging efficiencies of conventional nanoparticles due to the low accumulation in the tumor tissues. Such a fast phase-transformation behavior can strongly restrict the MNH within the tumor centers. Upon external magnetic irradiation, Zn ferrite MNPs obtained an enhanced heat transformation effect at a very low dosage due to its high SAR value and the linear self-assembly in the hydrogel environment under the ACMF, coupled with the heat accumulation *via* crosslinking among the nanoemulsion, so the MNH quickly produces large amounts of heat and dramatically raises the temperature of local tumor tissue, which can significantly cause tumor coagulation necrosis and completely eliminate tumors without reoccurrence. This first successful demonstration of a theranostic platform based on a unique surgical protocol using MNH provides an alternative way to improve the efficiency of therapy and the precision of the injection site, and shows great potential for clinical translation for efficient localized tumor therapy.

Acknowledgements

This research was supported by the National Basic Research Program of China (973 program No. 2013CB733800), the National Natural Science Foundation of China (No. 81571806,

81271677, 81671820), the Jiangsu Provincial Special Program of Medical Science (No. BL2013029), the Jiangsu Provincial Technical Innovation Fund for Scientific and Technological Enterprises (No. SBC201310643), a Talent 333 Project in Jiangsu Province (grant no. BRA2015492), and the National High Technology Research and Development Program of China (No. 2013AA032205).

Notes and references

1 P. Wust, B. Hildebrandt, G. Sreenivasa, B. Rau, J. Gellermann, H. Riess, R. Felix and P. M. Schlag, *Lancet Oncol.*, 2002, **3**, 487–497.
2 J.-P. Fortin, C. Wilhelm, J. Servais, C. Menager, J.-C. Bacri and F. Gazeau, *J. Am. Chem. Soc.*, 2007, **129**, 2628–2635.
3 S. Laurent, S. Dutz, U. O. Häfeli and M. Mahmoudi, *Adv. Colloid Interface Sci.*, 2011, **166**, 8–23.
4 C. S. S. R. Kumar and F. Mohammad, *Adv. Drug Delivery Rev.*, 2011, **63**, 789–808.
5 D. Yoo, J.-H. Lee, T.-H. Shin and J. Cheon, *Acc. Chem. Res.*, 2011, **44**, 863–874.
6 H. Huang, S. Delikanli, H. Zeng, D. M. Ferkey and A. Pralle, *Nat. Nanotechnol.*, 2010, **5**, 602–606.
7 J.-H. Lee, J.-T. Jang, J.-S. Choi, S. H. Moon, S.-H. Noh, J.-W. Kim, J.-G. Kim, I.-S. Kim, K. I. Park and J. Cheon, *Nat. Nanotechnol.*, 2011, **6**, 418–422.
8 K. Hayashi, M. Nakamura, H. Miki, S. Ozaki, M. Abe, T. Matsumoto, W. Sakamoto, T. Yogo and K. Ishimura, *Theranostics*, 2014, **4**, 834–844.
9 A. Espinosa, R. D. Corato, J. Kolosnjaj-Tabi, P. Flaud, T. Pellegrino and C. Wilhelm, *ACS Nano*, 2016, **10**, 2436–2446.
10 Y. P. Li, T.-Y. Lin, Y. Luo, Q. Q. Liu, W. W. Xiao, W. C. Guo, D. Lac, H. Y. Zhang, C. H. Feng, S. Wachsmann-Hogiu, J. H. Walton, S. R. Cherry, D. J. Rowland, D. Kukis, C. X. Pan and K. S. Lam, *Nat. Commun.*, 2014, **5**, 4712–4726.
11 N. Lee, D. Yoo, D. Ling, M. H. Cho, T. Hyeon and J. Cheon, *Chem. Rev.*, 2015, **115**, 10637–10689.
12 R. D. Corato, G. Bealle, J. Kolosnjaj-Tabi, A. Espinosa, O. Clement, A. K. A. Silva, C. Menager and C. Wilhelm, *ACS Nano*, 2015, **9**, 2904–2916.
13 K. Hayashi, M. Nakamura, W. Sakamoto, T. Yogo, H. Miki, S. Ozaki, M. Abe, T. Matsumoto and K. Ishimura, *Theranostics*, 2013, **3**, 366–376.
14 W. Hohenforst-Schmidt, P. Zarogoulidis, K. Darwiche, T. Vogl, E. P. Goldberg, H. Huang, M. Simoff, Q. Li, R. Browning, F. J. Turner, P. L. Pivert, D. Spyratos, K. Zarogoulidis, S. I. Celikoglu, F. Celikoglu and J. Brachmann, *Drug Des., Dev. Ther.*, 2013, **7**, 571–583.
15 O. L. Gobbo, K. Sjaastad, M. W. Radomski, Y. Volkov and A. Prina-Mello, *Theranostics*, 2015, **5**, 1249–1263.
16 K. Hayashi, W. Sakamoto and T. Yogo, *Adv. Funct. Mater.*, 2016, **26**, 1708–1718.
17 Y. Chen, L. Jiang, R. H. Wang, M. Lu, Q. X. Zhang, Y. Zhou, Z. G. Wang, G. M. Lu, P. Liang, H. T. Ran, H. R. Chen and Y. Y. Zheng, *Adv. Mater.*, 2014, **26**, 7468–7473.
18 P. Huang, J. Lin, W. W. Li, P. F. Rong, Z. Wang, S. J. Wang, X. P. Wang, X. L. Sun, M. Aronova, G. Niu, R. D. Leapman, Z. H. Nie and X. Y. Chen, *Angew. Chem., Int. Ed.*, 2013, **52**, 13958–13964.
19 J. Lin, M. Wang, H. Hu, X. Y. Yang, B. Wen, Z. T. Wang, O. Jacobson, J. B. Song, G. F. Zhang, G. Niu, P. Huang and X. Y. Chen, *Adv. Mater.*, 2016, **28**, 3273–3279.
20 T.-H. Shin, Y. Choi, S. Kim and J. Cheon, *Chem. Soc. Rev.*, 2015, **44**, 4501–4516.
21 X.-R. Song, X. Y. Wang, S.-X. Yu, J. B. Cao, S.-H. Li, J. Li, G. Liu, H.-H. Yang and X. Y. Chen, *Adv. Mater.*, 2015, **27**, 3285–3291.
22 J. E. Leslie-Barbick, J. E. Saik, D. J. Gould, M. E. Dickinson and J. L. West, *Biomaterials*, 2011, **32**, 5782–5789.
23 M. E. Helgeson, S. E. Moran, H. Z. An and P. S. Doyle, *Nat. Mater.*, 2012, **11**, 344–352.
24 J.-T. Jang, H. Nah, J.-H. Lee, S. H. Moon, M. G. Kim and J. Cheon, *Angew. Chem., Int. Ed.*, 2009, **48**, 1234–1238.
25 T. J. Wooster, M. Golding and P. Sanguansri, *Langmuir*, 2008, **24**, 12758–12765.
26 Y.-W. Jun, J.-H. Lee and J. Cheon, *Angew. Chem., Int. Ed.*, 2008, **47**, 5122–5135.
27 J. Xie, Y. Zhang, C. Y. Yan, L. N. Song, S. Wen, F. C. Zang, G. Chen, Q. Ding, C. Z. Yan and N. Gu, *Biomaterials*, 2014, **35**, 9126–9136.
28 K. Hu, J. F. Sun, Z. B. Guo, P. Wang, Q. Chen, M. Ma and N. Gu, *Adv. Mater.*, 2015, **27**, 2507–2514.
29 R. Hergt and S. Dutz, *J. Magn. Magn. Mater.*, 2007, **311**, 187–192.
30 L. C. Branquinho, M. S. Carriao, A. S. Costa, N. Zufelato, M. H. Sousa, R. Miotto, R. Ivkov and A. F. Bakuzis, *Sci. Rep.*, 2013, **3**, 2887–2897.
31 S. A. Stanley, J. E. Gagner, S. Damanpour, M. Yoshida, J. S. Dordick and J. M. Friedman, *Science*, 2012, **336**, 604–608.
32 K. F. Chu and D. E. Dupuy, *Nat. Rev. Cancer*, 2014, **14**, 199–208.

